University of Utrecht

Debye Institute

Nanophotonics Group

Numerical simulation of a spinor Bose-Einstein condensate.

Author:
Michał van Hooft

Supervisor:
Prof. Dr. Peter van der Straten

June 15, 2016

Abstract

The two-spin components Bose-Einstein condensate in simulated in an anisotropic harmonic potential. A reduced two-dimensional model for this system is developed. The ground state of the model is shown. In order to check the validity of the simulation the size of the interface of the condensate and the speed of sound in the condensate are calculated. The result show that the simulation correctly predicts the behavior of the BEC. The time evolution of the two-spin component Bose-Einstein condensate is investigated for a symmetrical and asymmetrical initial conditions. The results show that the components do not mix and slide past each other. The simulation predicts that the interface is turbulent during movement, but this might be due to the absence of dampening by a thermal cloud in the simulation.

Contents

1 Introduction

The Bose-Einstein condensate was predicted by Satyendra Bose and Albert Einstein in 1924. The idea resulted from Satyendra Bose deriving a quantum-mechanical proof for Planck's radiation law. This derivation was translated by Einstein into German and latter he expanded the idea to include matter as well. The Bose-Einstein condensate is formed by bosonic particles, particles that are allowed to be in the same quantum-mechanical state. By cooling these particles it is possible to make them occupy the lowest energy state of the system. If these particles are cooled enough, nearly all the particles condense into the lowest energy state and at this point they form a new form of matter called a Bose-Einstein condensate. The reason why Bose-Einstein condensates are interesting is because they form a macroscopic quantum-mechanical object and their unusual properties such as superfluity. In this thesis I will simulate a two-spin component Bose-Einstein condensate, where half of the particles in the condensate are transfered to another hyperfine state. The single spin component simulation already has theoretical framework [Weizhu Bao and Markowich(2003)] and a simulation of such a system has been done before [Pratama(2011)]. A two-spin component simulation has not been performed. In order to create the theoretical model for simulating a two spin component Bose-Einstein a model is developed along the lines of the single component model. Then the validity of the model is checked by comparing it with theoretical predictions for the speed of sound in the condensate and the width of the interface.

2 Theoretical model

2.1 Two-component Gross-Pitaevskii equations

The starting point of the numerical model used in the simulation are the generalized Gross-Pitaevskii equations for two interacting species. These equations will be derived along the lines of reference [Smith(2008)]. The first assumption made in the derivation of the Gross-Pitaevskii equations is that the complete quantum mechanical wave-function of the BEC may be written as a product of single particle wave-functions,

$$\psi(\boldsymbol{r_1}, ..., \boldsymbol{r_N}) = \prod_i^N \phi_1(\boldsymbol{r_i}). \tag{1}$$

Generalizing this assumption to two species we get: The complete wave-function may be written as a product of two single-species wave-functions,

$$\psi(\boldsymbol{r_1}, ..., \boldsymbol{r_{N_1}}, \boldsymbol{r'_1}, ..., \boldsymbol{r'_{N_2}}) = \prod_i^{N_1} \phi_1(\boldsymbol{r_i}) \prod_j^{N_2} \phi_2(\boldsymbol{r'_j}). \tag{2}$$

Both of the single particle states are normalized in the usual way, $\int |\phi_k(\boldsymbol{r})| d\boldsymbol{r} = 1$, with $k \in \{1,2\}$.This assumption is equivalent to a fully condensed state. Furthermore, the effective interaction between two species is calculated in reference [Smith(2008)] to be $U_0 \delta(\boldsymbol{r} - \boldsymbol{r'})$ with $U_0 = \frac{4\pi\hbar^2 a}{m}$. In the generalization the scattering length is dependent on the species in the interaction, so the coefficient in the interaction becomes:

$$U_{ij} = \frac{4\pi\hbar^2 a_{ij}}{m}. \tag{3}$$

At this point the Hamiltonian operator of the system may be written:

$$\begin{aligned} H = &\sum_i^{N_1} \frac{\boldsymbol{p}_i^2}{2m_1} + V_1(\boldsymbol{r_i}) + \sum_j^{N_2} \frac{\boldsymbol{p}_j^2}{2m_2} + V_2(\boldsymbol{r_j}) \\ &+ \sum_{i<k}^{N_1} U_{11} \delta(\boldsymbol{r}_i - \boldsymbol{r}_k) + \sum_{j<k}^{N_2} U_{22} \delta(\boldsymbol{r}_j - \boldsymbol{r}_k) + \sum_i^{N_1} \sum_j^{N_2} U_{12} \delta(\boldsymbol{r}_i - \boldsymbol{r}_j). \end{aligned} \tag{4}$$

Now the energy of the system is:

$$\begin{aligned} E &= \langle \psi | \, H \, | \psi \rangle \\ &= \int d\boldsymbol{r} \left[\frac{N_1 \hbar^2}{2m_1} |\nabla \psi_1|^2 + N_1 V_1(\boldsymbol{r}) |\psi_1|^2 + N_2 \frac{\hbar^2}{2m_2} |\nabla \psi_2|^2 + N_2 V_2(\boldsymbol{r}) |\psi_2|^2 \right. \\ &\left. + \frac{N_1(N_1-1)}{2} U_{11} |\psi_1|^4 + \frac{N_2(N_2-1)}{2} U_{22} |\psi_2|^4 + N_1 N_2 U_{12} |\psi_1|^2 |\psi_2|^2 \right]. \end{aligned} \tag{5}$$

Since N_1 and N_2 are large the approximation $\frac{N_2(N_2-1)}{2} \approx \frac{N_2^2}{2}$ holds. In order to simplify the equations, the particle number of the species is chosen to be equal, $N = N_1 = N_2$. The total amount of particles in the system becomes $2N$. Furthermore, the mass of the species is chosen to be equal, $m = m_1 = m_2$. The potential used is harmonic with a anisotropy in the y axis, $V_1 = V_2 = \frac{1}{2} m\omega_x^2 x^2 + \frac{1}{2} m\omega_y^2 y^2 + \frac{1}{2} m\omega_x^2 z^2$. Using all these assumptions the following equation for the energy is obtained from equation (5):

$$\begin{aligned} E = N \int d\boldsymbol{r} \left[\frac{\hbar^2}{2m} (|\nabla \phi_1|^2 + |\nabla \phi_2|^2) + (\frac{1}{2} m\omega_x^2 x^2 + \frac{1}{2} m\omega_y^2 y^2 + \frac{1}{2} m\omega_x^2 z^2)(|\phi_1|^2 + |\phi_2|^2) \right. \\ \left. + \frac{1}{2} \frac{4\pi\hbar^2 N a_{11}}{m} |\phi_1|^4 + \frac{1}{2} \frac{4\pi\hbar^2 N a_{22}}{m} |\phi_2|^4 + \frac{4\pi\hbar^2 N a_{12}}{m} |\phi_1|^2 |\phi_2|^2 \right]. \end{aligned} \tag{6}$$

2.2 Dimension reduction

In order to keep computation-time within practical limits it is necessary to reduce the final model to two dimensions. This is done along the lines of reference [L. Salasnich and Reatto(2002)]. The main idea in this technique is to choose a distribution in the dimensions you want to reduce. This distribution is influenced by a width parameter $\eta(x,y,t)$ that is itself dependent on the other dimensions or in mathematical terms:

$$\phi_1(x,y,z,t) = f(z,t,\eta(x,y,t))\phi_1'(x,y,t), \tag{7}$$

$$\phi_2(x,y,z,t) = f(z,t,\eta(x,y,t))\phi_2'(x,y,t), \tag{8}$$

$$f(z,t,\eta(x,y,t)) = \frac{e^{\frac{-z^2}{2\eta^2}}}{\pi^{\frac{1}{4}}\eta^{\frac{1}{2}}}. \tag{9}$$

The choice for $f(z,t,\eta(x,y,t))$ is the ground state of the harmonic oscillator with a variable width $\eta(x,y,t)$. While the Gaussian distribution is not the only choice and a Thomas-Fermi profile might be a better approximation, this is easier to work with mathematically and the Thomas-Fermi profile is based on the absence of kinetic energy. Therefore it does not work in regimes where kinetic energy is dominant. Furthermore, $\frac{1}{\pi^{\frac{1}{4}}\eta^{\frac{1}{2}}}$ is the normalizing constant to ensure: $\int_{-\infty}^{\infty} f^2 dz = 1$ holds. For the next step the equations (7) and (8) are inserted into the equation for the energy (6):

$$\begin{aligned} E = N\int d\boldsymbol{r}\Bigg[& \frac{-\hbar^2}{2m}(f{\phi'}_1^*\Delta(f\phi_1') + f{\phi'}_2^*\Delta(f\phi_2')) \\ & + \left((\frac{1}{2}m\omega_x^2x^2 + \frac{1}{2}m\omega_y^2y^2 + \frac{1}{2}m\omega_x^2z^2)(|\phi_1'|^2 + |\phi_2'|^2)\right) f^2 \\ & + \left(\frac{1}{2}\frac{4\pi\hbar^2Na_{11}}{m}|\phi_1'|^4 + \frac{1}{2}\frac{4\pi\hbar^2Na_{22}}{m}|\phi_2'|^4 + \frac{4\pi\hbar^2Na_{12}}{m}|\phi_1'|^2|\phi_2'|^2\right) f^4\Bigg]. \end{aligned} \tag{10}$$

The primes are left out for simplicity. The distribution $f(z,t,\eta(x,y,t))$ is most strongly dependent in z. So

$$\Delta(f\phi_i) \approx \phi_i\frac{\partial^2 f}{\partial z^2} + f\Delta_\perp\phi_i, \tag{11}$$

where $\Delta_\perp = \frac{\partial^2}{\partial x^2} + \frac{\partial^2}{\partial y^2}$. The integrals that appear in equation 10 can be evaluated:

$$\int dz f^2 = 1, \tag{12}$$

$$\int dz f^2 z^2 = \frac{\eta^2}{2}, \tag{13}$$

$$\int dz f^4 = \frac{1}{\sqrt{2\pi}\eta}, \tag{14}$$

$$\int dz f\frac{\partial^2 f}{\partial z^2} = \frac{-1}{2\eta^2}. \tag{15}$$

Thus the energy is obtained from equation (10):

$$\begin{aligned} E = N\int dxdy\Bigg[& \frac{-\hbar^2}{2m}(\phi_1^*\Delta_\perp\phi_1 + \phi_2^*\Delta_\perp\phi_2 - \frac{(|\phi_1|^2 + |\phi_2|^2)}{2\eta^2}) \\ & + (\frac{1}{2}m\omega_x^2x^2 + \frac{1}{2}m\omega_y^2y^2)(|\phi_1|^2 + |\phi_2|^2) + \frac{m\omega_x^2\eta^2(|\phi_1|^2 + |\phi_2|^2)}{4} \\ & + \frac{\sqrt{2\pi}\hbar^2Na_{11}}{m\eta}|\phi_1|^4 + \frac{\sqrt{2\pi}\hbar^2Na_{22}}{m\eta}|\phi_2|^4 + \frac{2\sqrt{2\pi}\hbar^2Na_{12}}{m\eta}|\phi_1|^2|\phi_2|^2\Bigg]. \end{aligned} \tag{16}$$

To find solutions for ϕ_1 and ϕ_2 the energy, E, is minimized with respect to ϕ_1, ϕ_1^*, ϕ_2, ϕ_2^* and η with the restrictions $\int |\phi_1|^2 d\boldsymbol{r} = 1$ and $\int |\phi_2|^2 d\boldsymbol{r} = 1$. This is done by using Lagrange multipliers μ_1 and μ_2 that are the chemical potential of species one and two. In mathematical terms this must be solved:

$$\delta E - \mu_1 \delta N_1 - \mu_2 \delta N_2 = 0. \tag{17}$$

Here δ represents the functional derivative to either ϕ_1^*, ϕ_2^* or η. The derivatives to ϕ_1 and ϕ_2 yield the same equations as the derivatives to the conjugates, so are left out. Equation 17 yields:

$$\begin{aligned} N\mu_1\phi_1 = \frac{\delta E}{\delta \phi_1^*} = \Bigg(& \frac{-\hbar^2}{2m}\left(\frac{\partial^2}{\partial x^2} + \frac{\partial^2}{\partial y^2}\right) + \frac{\hbar^2}{4m\eta^2} + \frac{1}{2}m\omega_x^2 x^2 + \frac{1}{2}m\omega_y^2 y^2 \\ & + \frac{m\omega_x^2\eta^2}{4} + \frac{2\sqrt{2\pi}\hbar^2 N a_{11}}{m\eta}|\phi_1|^2 + \frac{2\sqrt{2\pi}\hbar^2 N a_{12}}{m\eta}|\phi_2|^2 \Bigg)\phi_1 N, \end{aligned} \tag{18}$$

$$\begin{aligned} N\mu_2\phi_2 = \frac{\delta E}{\delta \phi_2^*} = \Bigg(& \frac{-\hbar^2}{2m}\left(\frac{\partial^2}{\partial x^2} + \frac{\partial^2}{\partial y^2}\right) + \frac{\hbar^2}{4m\eta^2} + \frac{1}{2}m\omega_x^2 x^2 + \frac{1}{2}m\omega_y^2 y^2 \\ & + \frac{m\omega_x^2\eta^2}{4} + \frac{2\sqrt{2\pi}\hbar^2 N a_{22}}{m\eta}|\phi_2|^2 + \frac{2\sqrt{2\pi}\hbar^2 N a_{12}}{m\eta}|\phi_1|^2 \Bigg)\phi_2 N, \end{aligned} \tag{19}$$

$$\begin{aligned} 0 = \frac{\delta E}{\delta \eta} = & -\frac{\hbar^2(|\phi_1|^2 + |\phi_2|^2)}{2m\eta^3} + \frac{m\omega_x^2\eta(|\phi_1|^2 + |\phi_2|^2)}{2} \\ & - \frac{\sqrt{2\pi}\hbar^2 N a_{11}}{m\eta^2}|\phi_1|^4 - \frac{\sqrt{2\pi}\hbar^2 N a_{22}}{m\eta^2}|\phi_2|^4 - \frac{2\sqrt{2\pi}\hbar^2 N a_{12}}{m\eta^2}|\phi_1|^2|\phi_2|^2. \end{aligned} \tag{20}$$

Equation (20) is used to solve for η. We assume that for the purpose of η the scattering lengths are identical, $a_{11} \approx a_{12} \approx a_{22}$. Using this some terms from equation (20) may be simplified to:

$$\begin{aligned} & \frac{\sqrt{2\pi}\hbar^2 N a_{11}}{m\eta^2}|\phi_1|^4 + \frac{\sqrt{2\pi}\hbar^2 N a_{22}}{m\eta^2}|\phi_2|^4 + \frac{2\sqrt{2\pi}\hbar^2 N a_{12}}{m\eta^2}|\phi_1|^2|\phi_2|^2 \\ & = \frac{\sqrt{2\pi}\hbar^2 N a_{11}}{m\eta^2}(|\phi_1|^2 + |\phi_2|^2)^2. \end{aligned}$$

So the equation (20) reduces to:

$$0 = -\frac{\hbar^2(|\phi_1|^2 + |\phi_2|^2)}{2m\eta^3} + \frac{m\omega_x^2\eta(|\phi_1|^2 + |\phi_2|^2)}{2} - \frac{\sqrt{2\pi}\hbar^2 N a_{11}}{m\eta^2}(|\phi_1|^2 + |\phi_2|^2)^2, \tag{21}$$

or

$$\frac{\sqrt{2\pi}\hbar^2 N a_{11}}{m}(|\phi_1|^2 + |\phi_2|^2) = -\frac{\hbar^2}{2m\eta} + \frac{m\omega_x^2\eta^3}{2}. \tag{22}$$

There exists a exact solution for equation (22). But this solution involves many roots and this is not preferable for numerical simulations. Thus the solution is split into two regimes. In the first regime kinetic energy is negligible, while in the second the density of the condensate is nearly zero. Thus using this approximation the following solutions are obtained:

$$\eta_1^3 = \frac{2\sqrt{2\pi}\hbar^2 N a_{11}}{m^2\omega_x^2}(|\phi_1|^2 + |\phi_2|^2), \tag{23}$$

$$\eta_2 = \sqrt{\frac{\hbar}{m\omega_x}}. \tag{24}$$

In order to provide a smooth solution for η, η is chosen the square root of the sum of the squares of both solutions,

$$\eta = \sqrt{\eta_1^2 + \eta_2^2}. \tag{25}$$

The kinetic term ensures that η can not drop below the width of the ground state of the harmonic oscillator. In order to obtain the time evolution equations, the time-dependent generalization of the Schrödinger equation is used. So the final equations are:

$$\begin{aligned} i\hbar\frac{\partial\phi_1}{\partial t} = \Bigg(&\frac{-\hbar^2}{2m}\left(\frac{\partial^2}{\partial x^2}+\frac{\partial^2}{\partial y^2}\right)+\frac{\hbar^2}{4m\eta^2}+\frac{1}{2}m\omega_x^2x^2+\frac{1}{2}m\omega_y^2y^2 \\ &+\left(\frac{m\omega_x^2\eta^2}{4}+\frac{2\sqrt{2\pi}\hbar^2Na_{11}}{m\eta}|\phi_1|^2+\frac{2\sqrt{2\pi}\hbar^2Na_{12}}{m\eta}|\phi_2|^2\right)\Bigg)\phi_1, \end{aligned} \tag{26}$$

$$\begin{aligned} i\hbar\frac{\partial\phi_2}{\partial t} = \Bigg(&\frac{-\hbar^2}{2m}\left(\frac{\partial^2}{\partial x^2}+\frac{\partial^2}{\partial y^2}\right)+\frac{\hbar^2}{4m\eta^2}+\frac{1}{2}m\omega_x^2x^2+\frac{1}{2}m\omega_y^2y^2 \\ &+\frac{m\omega_x^2\eta^2}{4}+\frac{2\sqrt{2\pi}\hbar^2Na_{22}}{m\eta}|\phi_2|^2+\frac{2\sqrt{2\pi}\hbar^2Na_{12}}{m\eta}|\phi_1|^2\Bigg)\phi_2. \end{aligned} \tag{27}$$

Equations (26) and (27) together with equation (25) are solved using numerical simulation.

2.3 Scaling

Equations (26) and (27) may be scaled to make the inner workings of the simulation easier to understand. The position x is scaled with the estimated length of the system x_s. y is scaled with $\frac{\omega_x}{\omega_y}x_s$. The time, t, is scaled with ω_x. Furthermore, due to the scaling of x and y, ϕ_1 and ϕ_2 must be scaled too in order for the integral $\int |\phi_1|^2 dxdy = 1$ to be preserved. So this will result in new dimensionless quantities t', x', y' , ϕ_1' and ϕ_2' defined by:

$$t' = \omega_x t, \tag{28}$$

$$x' = \frac{x}{x_s}, \tag{29}$$

$$y' = \frac{\omega_y}{\omega_x}\frac{y}{x_s}, \tag{30}$$

$$\phi_1' = \phi_1 x_s \sqrt{\frac{\omega_x}{\omega_y}}, \tag{31}$$

$$\phi_2' = \phi_2 x_s \sqrt{\frac{\omega_x}{\omega_y}}. \tag{32}$$

Equations (26) and (27) are divided by $\hbar\omega_x$. A new dimensionless parameter $\eta' = \eta/x_s$ is introduced. Furthermore, we define $A = \frac{\hbar}{m x_s^2 \omega_x}$ and $\kappa_{ij} = \frac{2\sqrt{2\pi}\hbar N a_{ij}\omega_y}{m x_s^3 \omega_x^2}$. Using all the previous steps a new formulation of equations (26) and (27) is obtained:

$$\begin{aligned} i\frac{\partial\phi_1}{\partial t} = &\left(\frac{-A}{2}\left(\frac{\partial^2}{\partial x^2} + \frac{\omega_y^2}{\omega_x^2}\frac{\partial^2}{\partial y^2}\right) + \frac{A}{4\eta'^2} + \frac{1}{2A}(x^2+y^2) + \frac{\eta'^2}{4A}\right. \\ &\left. + \frac{\kappa_{11}}{\eta'}|\phi_1'|^2 + \frac{\kappa_{12}}{\eta'}|\phi_2'|^2\right)\phi_1', \end{aligned} \tag{33}$$

$$\begin{aligned} i\frac{\partial\phi_2}{\partial t} = &\left(\frac{-A}{2}\left(\frac{\partial^2}{\partial x^2} + \frac{\omega_y^2}{\omega_x^2}\frac{\partial^2}{\partial y^2}\right) + \frac{A}{4\eta'^2} + \frac{1}{2A}(x^2+y^2) + \frac{\eta'^2}{4A}\right. \\ &\left. + \frac{\kappa_{22}}{\eta'}|\phi_2'|^2 + \frac{\kappa_{12}}{\eta'}|\phi_1'|^2\right)\phi_2', \end{aligned} \tag{34}$$

$$\eta_1'^3 = \kappa_{11} A(|\phi_1'|^2 + |\phi_2'|^2), \tag{35}$$

$$\eta_2'^2 = A, \tag{36}$$

$$\eta' = \sqrt{\eta_1'^2 + A}\ . \tag{37}$$

Due to the scaling, the energy and force are dimensionless. In order to compute the real energy from the dimensionless energy it must be multiplied by $\hbar\omega_x$, $E = \hbar\omega_x E'$. To compute forces in the x direction: $F_y = F_y' \frac{\hbar\omega_x}{x_s}$. And in the y direction: $F_x = F_x' \frac{\hbar\omega_y}{x_s}$.

2.4 Time-splitting method

In order to make use of these equations for numerical simulation the time splitting method as described in reference [Weizhu Bao and Markowich(2003)] is used. The idea of time splitting method is to look at an equation of the form:

$$\frac{\partial f(t)}{\partial t} = A(f(t)) + B(f(t)), \tag{38}$$

with A and B operators. Then approximate the solution to equation (38) a time step Δt further with $E_A(E_B(f(t)))$, where E_A and E_B are the operators that transform $f(t)$ to the exact solution $f(t+\Delta t)$ for the equations $\frac{\partial f(t)}{\partial t} = A(f(t))$ and $\frac{\partial f(t)}{\partial t} = B(f(t))$.
In order to apply the same method to equations (33) and (34), we start with defining the operators G_1, G_2 and K:

$$G_1(x,y) = \frac{A}{4\eta^2} + \frac{1}{2A}(x^2+y^2) + \frac{\eta^2}{4A} + \frac{\kappa_{11}}{\eta}|\phi_1|^2 + \frac{\kappa_{12}}{\eta}|\phi_2|^2, \tag{39}$$

$$G_2(x,y) = \frac{A}{4\eta^2} + \frac{1}{2A}(x^2+y^2) + \frac{\eta^2}{4A} + \frac{\kappa_{22}}{\eta}|\phi_2|^2 + \frac{\kappa_{12}}{\eta}|\phi_1|^2, \tag{40}$$

$$K(x,y) = \frac{-A}{2}\left(\frac{\partial^2}{\partial x^2} + \frac{\omega_y^2}{\omega_x^2}\frac{\partial^2}{\partial y^2}\right). \tag{41}$$

Note that with the operators equations (33) and (34) become

$$i\frac{\partial \phi_1}{\partial t} = \frac{G_1}{2}\phi_1 + K\phi_1 + \frac{G_1}{2}\phi_1, \tag{42}$$

$$i\frac{\partial \phi_2}{\partial t} = \frac{G_2}{2}\phi_2 + K\phi_2 + \frac{G_2}{2}\phi_2. \tag{43}$$

The time is discretized into intervals $[t_m, t_{m+1}]$ with $t_m = m\Delta t$. Now it is assumed the operators G_1, G_2 and K are independent of time during each time step. This gives the exact solution to the equations

$$i\frac{\partial \phi_1}{\partial t} = \frac{G_1(t_m,x,y)}{2}\phi_1, \tag{44}$$

$$i\frac{\partial \phi_2}{\partial t} = \frac{G_2(t_m,x,y)}{2}\phi_2 \tag{45}$$

to be:

$$\phi_1(t_{m+1},x,y) = e^{\frac{-i\Delta t G_1(t_m,x,y)}{2}}\phi_1(t_m,x,y) = E_{G_1}(t_m,x,y)\phi_1(t_m,x,y), \tag{46}$$

$$\phi_2(t_{m+1},x,y) = e^{\frac{-i\Delta t G_2(t_m,x,y)}{2}}\phi_2(t_m,x,y) = E_{G_2}(t_m,x,y)\phi_2(t_m,x,y). \tag{47}$$

Here the solution operators $E_{G_1}(t_m,x,y)$ and $E_{G_2}(t_m,x,y)$ are defined. To find the exact solution to

$$i\frac{\partial \phi_i}{\partial t} = K\phi_i = \frac{-A}{2}\left(\frac{\partial^2}{\partial x^2} + \frac{\omega_y^2}{\omega_x^2}\frac{\partial^2}{\partial y^2}\right)\phi_i, \tag{48}$$

a Fourier-transform must be performed,

$$\hat{\phi}_i(t_m,k_x,k_y) = \mathcal{F}(\phi_i) = \int_{-\infty}^{\infty}\int_{-\infty}^{\infty}\phi_i(t_m,x,y)e^{-i(k_x x + k_y y)}dxdy. \tag{49}$$

When the Fourier integration is performed on both sides of (48) one obtains:

$$\mathcal{F}\left(i\frac{\partial \phi_i}{\partial t}\right) = i\frac{\partial \hat{\phi}_i}{\partial t} = \hat{K}\hat{\phi}_i = \mathcal{F}(K\phi_i), \tag{50}$$

where $\hat{K} = \frac{A}{2}(k_x^2 + \frac{\omega_y^2}{\omega_x^2}k_y^2)$. Which has the solution

$$\hat{\phi}_i(t_{m+1}, k_x, k_y) = \hat{\phi}_i(t_m, k_x, k_y)e^{-i\Delta t\hat{K}} = E_{\hat{K}}(t_m, k_x, k_y)\hat{\phi}_i(t_m, k_x, k_y). \tag{51}$$

So the solution to equation (48) is a Fourier-forward transform,$\mathcal{F}$, then performing the kinetic solution operator ,$E_{\hat{K}}$, and then Fourier transforming back,$\mathcal{F}^{-1}$. By applying the solutions $E_{G_1}(t_m, x, y)$, $E_{G_2}(t_m, x, y)$ and $\mathcal{F}^{-1}$ $E_{\hat{K}}$ $\mathcal{F}$ after each other the full procedure of a time step is obtained. In the real simulation the space discretized versions of these operators are used.

2.5 Full procedure of a timestep

Given a mesh x_n and y_n with $n \in [0 : xMesh \times yMesh]$. We introduce the notation $E_{G_1,n} = E_{G_1}(t_m, x_n, y_n)$, $E_{G_2,n} = E_{G_2}(t_m, x_n, y_n)$ and $E_{\hat{K},n} = E_{\hat{K}}(t_m, x_n, y_n)$. The full procedure of a time-step done in the simulation is:

1: for all n: Compute η using formula (37).
2: for all n: $\phi^\circ_{1,n}(t_m) = E_{G_1,n}\phi_{1,n}(t_m)$ and $\phi^\circ_{2,n}(t_m) = E_{G_2,n}\phi_{2,n}(t_m)$.
3: Fourier transform: $\hat{\phi_1} = \mathcal{F}(\phi^\circ_1)$ and $\hat{\phi_2} = \mathcal{F}(\phi^\circ_2)$.
4: for all n : $\hat{\phi}_{1,n}(t_{m+1}) = E_{\hat{K},n}\hat{\phi}_{1,n}(t_m)$ and $\hat{\phi}_{2,n}(t_{m+1}) = E_{\hat{K},n}\hat{\phi}_{2,n}(t_m)$.
5: Fourier transform: $\phi^\circ_1 = \mathcal{F}^{-1}(\hat{\phi_1})$ and $\phi^\circ_2 = \mathcal{F}^{-1}(\hat{\phi_2})$.
6: Normalize ϕ°_1 and ϕ°_2
7: for all n: Compute η using formula (37).
8: for all n: $\phi_{1,n}(t_{m+1}) = E_{G_1,n}\phi^\circ_{1,n}(t_m)$ and $\phi_{2,n}(t_{m+1}) = E_{G_2,n}\phi^\circ_{2,n}(t_m)$.
9: Normalize ϕ_1 and ϕ_2.

In the actual simulation it suffices to keep two fields per species. One with the state of the wave function in real space and one in Fourier-space. The renormalization is not necessary in real time evolution, but it is in imaginary time evolution as explained in the next section.

2.6 Imaginary time evolution

In order to find the ground state of the system imaginary time evolution may be used. First it is assumed that the wave function is in a linear superposition of states, ψ_k, with energy E_k. Then the time t is substituted to $-it$ such that in the time evolution the higher order parts decay exponentially. Or in mathematical terms:

$$\phi(t, x, y) = \sum_k C_k\psi_k(x, y)e^{-iE_kt}, \tag{52}$$

where $C_k \in \mathbb{C}$. So after substituting imaginary time:

$$\phi(t, x, y) = \sum_k C_k\psi_k(x, y)e^{-E_kt}. \tag{53}$$

So the states with higher energy decay faster. Combined with the normalization imaginary time evolution converges to the ground state. Yet there is an important note: this procedure amuses there is a nonzero part of the ground state. So it is still important too choose the initial state wisely. Typically the starting condition is a Gaussian profile centered in the origin.

3 Results

3.1 Constants used

Unless noted otherwise the constants of the simulation are:

Constant	Value	Description
N	1.08×10^9 particles	The amount of particles
m	$3.817\,540\,5 \times 10^{-26}\,\mathrm{kg}$	The mass of a sodium atom
$\omega_x/2\pi$	$104\,\mathrm{Hz}$	Trap frequency in x and z direction
$\omega_y/2\pi$	$10\,\mathrm{Hz}$	trap frequency in y direction
a_{11}	$2.803\,580\,86 \times 10^{-9}\,\mathrm{m}$	Scattering length species one
a_{12}	$2.803\,580\,86 \times 10^{-9}\,\mathrm{m}$	Scattering length interaction
a_{22}	$2.704\,248 \times 10^{-9}\,\mathrm{m}$	Scattering length species two
x_s	$1 \times 10^{-6}\,\mathrm{m}$	Scaling parameter

Furthermore, for the simulation there are settings that are used and quantities of the simulation. The first column of the underlying table contains the constants in the scaled equation and the right column contains their unscaled counterpart.

Scaled	Value	Variable	Value	comment
x'_{size}	140	x_{size}	140 μm	Size of system in x
y'_{size}	140	y_{size}	1456 μm	Size of system in y
$\Delta t'$	3×10^{-3}	Δt	4.6 μs	Imaginary Time evolution
$\Delta t'$	2×10^{-4}	Δt	0.31 μs	Real Time evolution
x_{Mesh}	375	dx	0.37 μm	Distance between 2 grid points
y_{Mesh}	2025	dy	0.69 μm	Distance between 2 grid points

The coherence length or healing in the system is the length scale at which a disturbance returns to its bulk value. The coherence length in the center of the condensate under these conditions is given by [Smith(2008)]:

$$\epsilon = \sqrt{\frac{1}{8\pi n a_{11}}} = 0.0973\,\mu\mathrm{m}. \tag{54}$$

The mesh-sizes are odd numbers, because in order to make the grid with a origin symmetric around the origin a uneven number of point is necessary. The Fourier-transformations is written out explicitly in multiples of small factors, therefore to make to simulation faster it is chosen as a multiple of these.

3.2 Imaginary time evolution

When showing results there are two different options. The computations use a two-dimensional wave function as defined in equation (33). This method represents the data in density per squared meter and the result is shown in figure 1. This is equivalent to what is observed in a experimental setup if the absorption is measured with a single camera. The drawback is that this is not physical quantity. The other way of showing the result is an intersection at a certain z-plane which is chosen to be the $z = 0$ plane. This approach is shown in figure 2. Since both show approximately the same result, it is chosen to only show the result of the intersection in the next sections. Furthermore, the real ratio between the x an y coordinate is approximately 10, while the ratio shown in the results is 5.

In figure 1 it may be seen that the second particle sits in the center of the potential while the

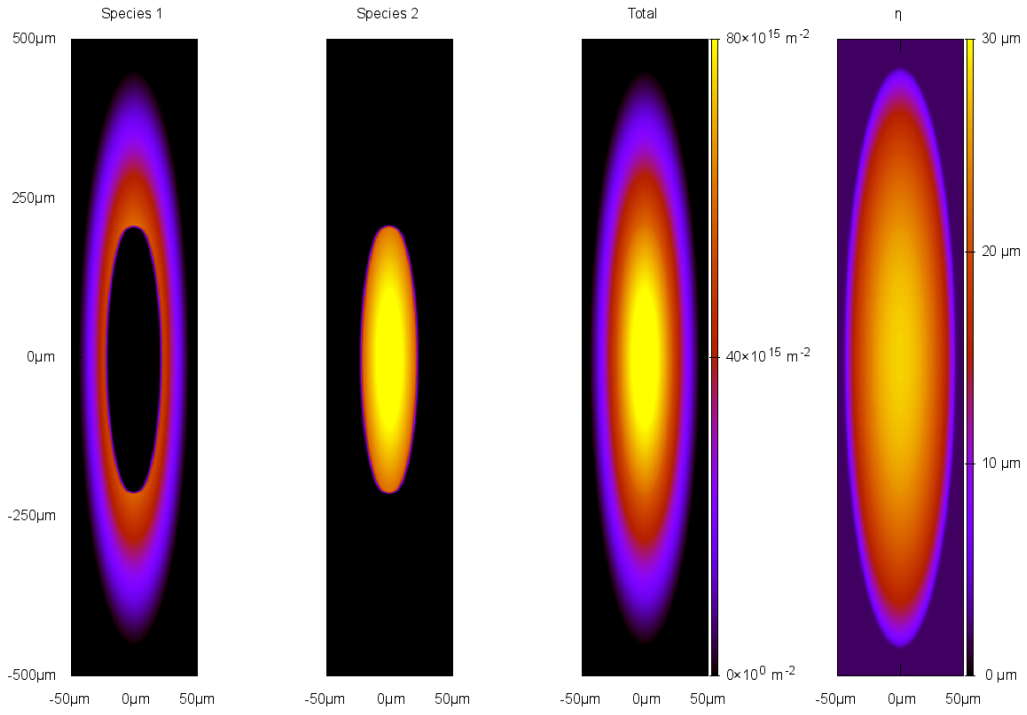

Figure 1: The result of 10000 steps imaginary time evolution with $M'_y = 0$. With mesh size 375×2025 ,$\mu'_1 = 227.397 \pm 0.005$ and $\mu'_2 = 224.859 \pm 0.006$. How the chemical potential and its variation are calculated is explained in section 3.3.

first particle occupies the space around it. The reason for this is: The second species has a lower scattering-length, so its self-interaction is lower than that of the other particle. Due to the lower self-interaction it is energetically favorable to occupy the center where the density is higher and it can profit from the lower self-interaction compared to the first species.

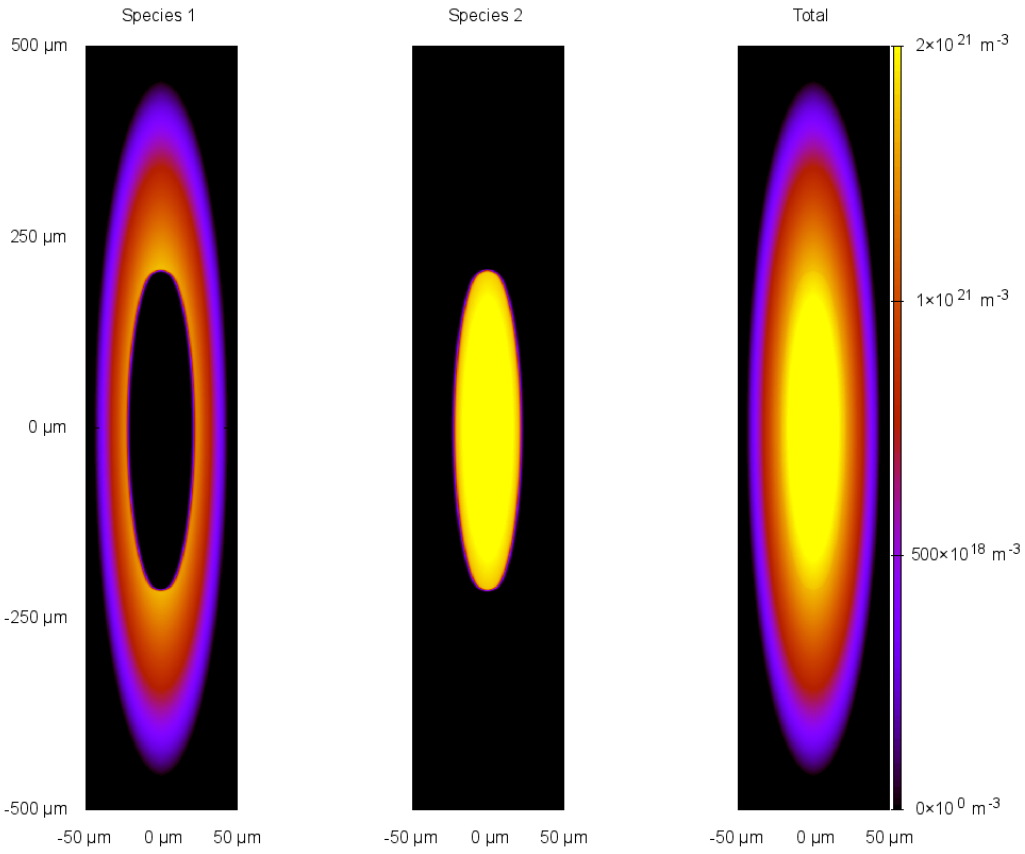

Figure 2: The same conditions as figure 1 except that here the density is shown at $z = 0$ plane

If a small spin dependent force is introduced by changing the potential to

$$V_1(x,y) = \frac{(x^2 + M'_x x + {M'_x}^2) + (y^2 + M'_y y + {M'_y}^2)}{2A}, \tag{55}$$

$$V_2(x,y) = \frac{(x^2 - M'_x x + {M'_x}^2) + (y^2 - M'_y y + {M'_y}^2)}{2A}, \tag{56}$$

the result completely changes the as is seen in figure 3. With the force in the y direction $M'_y = 1.0$ and the force in the x direction $M'_x = 0$. These are the default conditions for the rest of the thesis. Surprisingly the chemical potential of the state without spin dependent force has a higher chemical potential than the state with a spin dependent force. The first species has a chemical potential, μ'_1, of 227.397 ± 0.005 in the first state and 226.008 ± 0.002 in the second state. The second species has a chemical potential, μ'_2, of 224.859 ± 0.006 in the first state and 223.250 ± 0.002 in the second state. The addition of the force did not lower the chemical potential by shifting zero level of the potential. Since the equation (55) ensures that the minimum is above zero, so adding the spin dependent force did not lower the chemical potential. How the chemical potential and its error are calculated is explained in the next section.

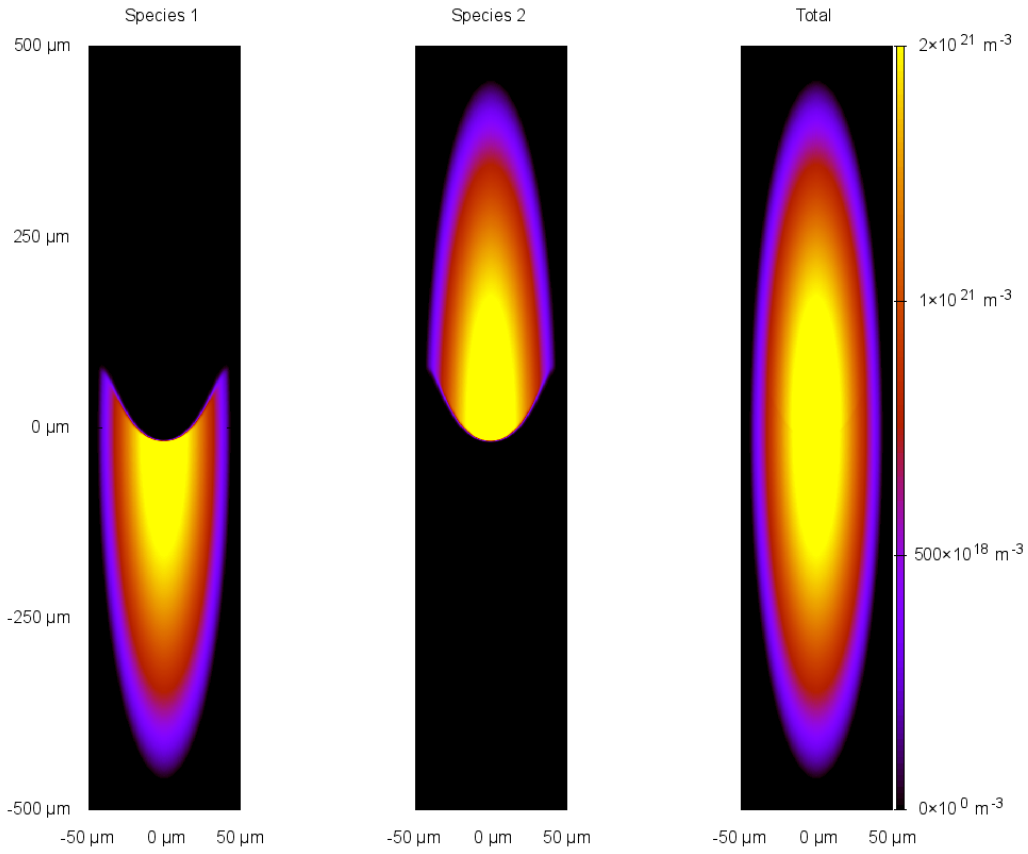

Figure 3: The result of 10000 steps imaginary time evolution with $M_y' = 1.0$. With mesh 375×2025 , $\mu_1' = 226.008 \pm 0.002$ and $\mu_2' = 223.250 \pm 0.002$.

3.3 Convergence and validity of imaginary time evolution

To show that figures 1 and 3 are indeed steady states, the chemical potential is computed at each lattice site. By dividing equation (18) by $N\phi_1$, μ_1 is obtained on each lattice site. The result is shown in figure 4. Using this method an average and a variation with the density at the site as a weight is computed. This result is shown as a function of time in figures 5 and 6 , both the variation and energy decay exponentially. The energy itself keeps converging until numerical noise kicks in. The variation becomes constant earlier. The reason is the noise around the condensate. As seen in figure 4 the chemical potential is constant at the places where the density is large. But it is non constant at places where the density is low. This effect does not disappear when the imaginary time evolution runs longer. The cause of this behavior is not clear, but probably does not significantly affect the simulation.

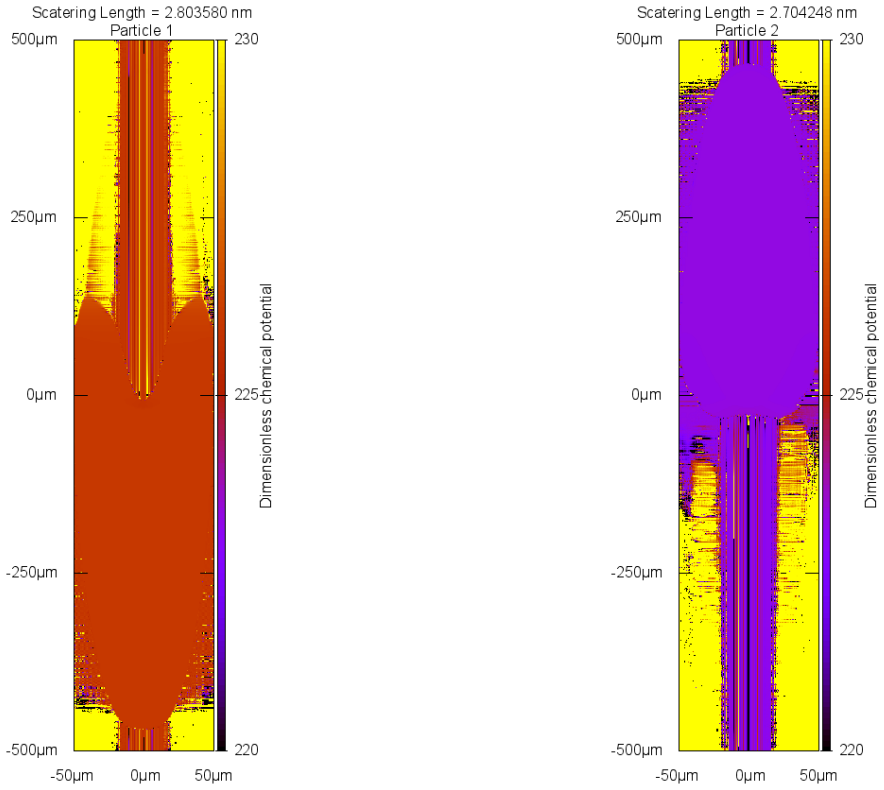

Figure 4: Dimensionless chemical potential calculated at each lattice site for a steady state with spin dependent force $M_y' = 1.0$.

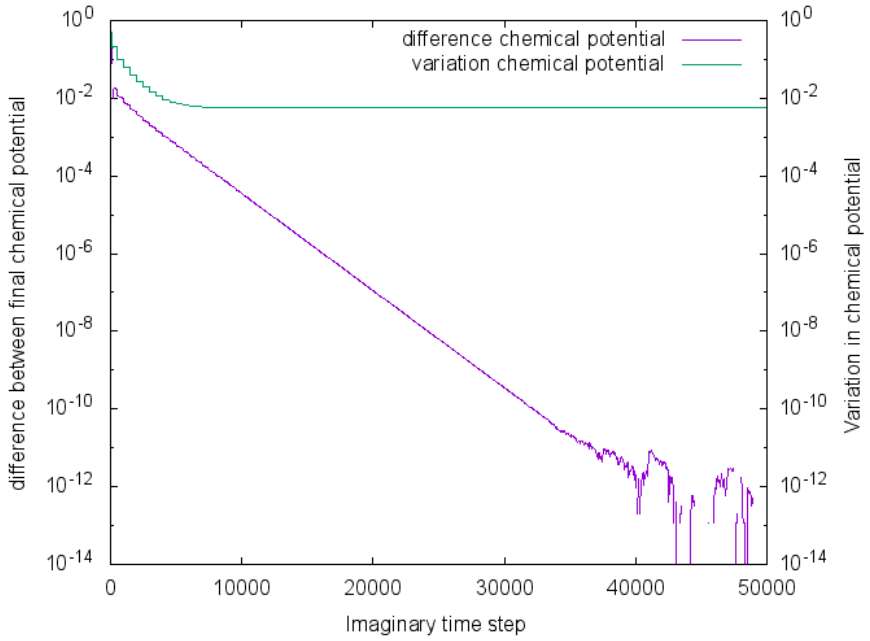

Figure 5: The average and variation in chemical potential as a function of imaginary time step, without spin dependent force. The step function like behavior in the variation is because the imaginary time steps are made smaller and the time steps after a lowering of Δt give a large increase in accuracy.

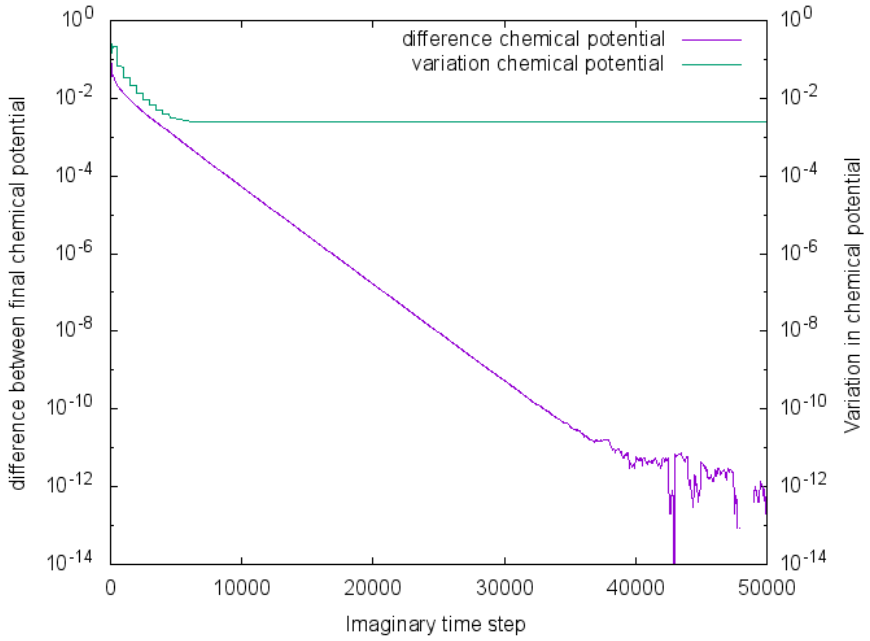

Figure 6: The average and variation in chemical potential as a function of imaginary time step ,with spin dependent force. The step function like behavior in the variation is because the imaginary time steps are made smaller and the time steps after a lowering of Δt give a large increase in accuracy.

3.4 The interface

Between different components of the condensate an interface is formed. In the current situation of the condensate the dominant forces are the self interaction and the potential field. Near the interface kinetic energy becomes relevant. The interface is shown in good detail in figures 7, 8 and 9. The

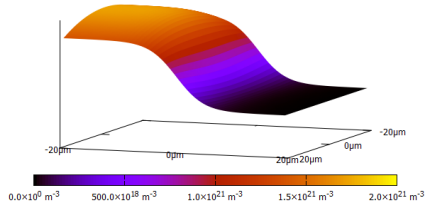

Figure 7: The interface at $(a_{11} - a_{22}) = 0.0025\,\text{nm}$

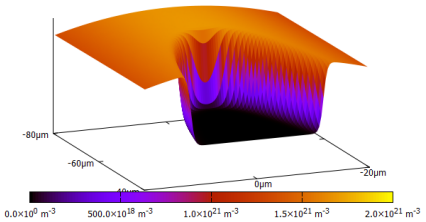

Figure 9: The interface at $(a_{11} - a_{22}) = 0.16\,\text{nm}$

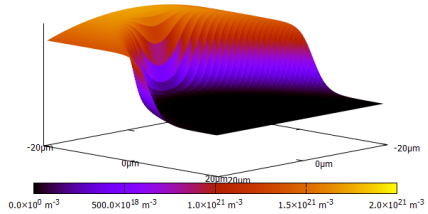

Figure 8: The interface at $(a_{11} - a_{22}) = 0.0361\,\text{nm}$

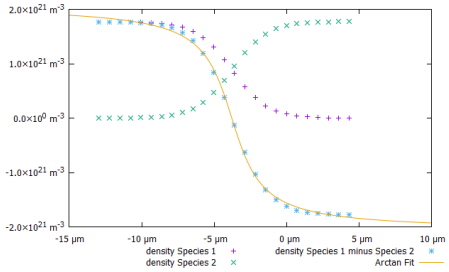

Figure 10: Intersection trough the center of the condensate at with: $(a_{11} - a_{22}) = 0.01\,\text{nm}$

results may be compared to that of theoretical models. The first prediction is that the shape of the interface is an arctangent [Corver(2015)]. This is seen in figure 10 where the density at the interface is fitted with an arctangent. Another theoretical prediction is that of the spin-healing length ϵ_s is given by [Matuszewski(2010)]:

$$\epsilon_s = \frac{\sqrt{\pi}}{\sqrt{\frac{2}{3}n(a_{11} - a_{22})}}. \tag{57}$$

The ground state is computed for many different scattering lengths ,$(a_{11} - a_{22})$, and the intersection through the center may be fitted with

$$P(x) = A\arctan(\sqrt{2\pi}\frac{(x - C)}{B}). \tag{58}$$

The results of this procedure are shown in figure 11. The uncertainty is estimated from the asymptotic standard error of the fit.

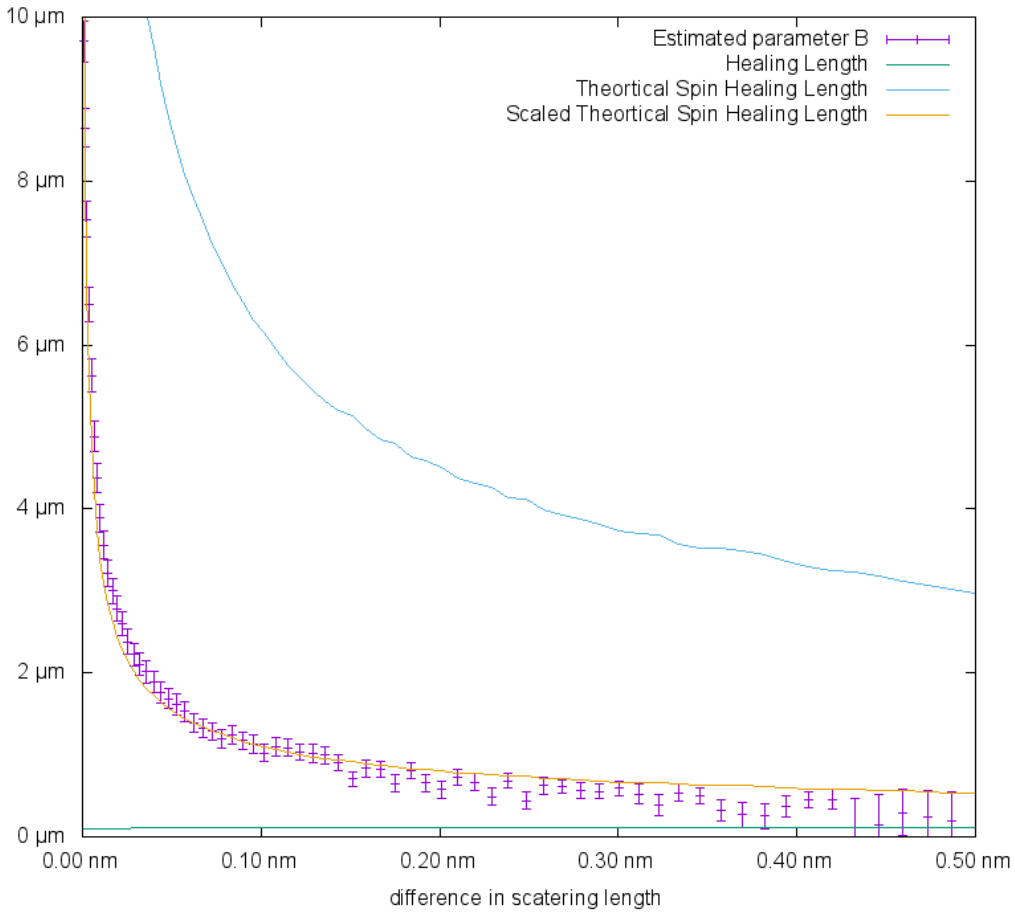

Figure 11: The results of of fitting formula 58 with A,B and C compared with the theoretical prediction and scaled theoretical prediction.

The results of figure 11 do not agree with the theoretical prediction, but when the results of figure 11 are compared with a multiple of the theoretical result, the results agree within errorbars. So the relation of equation (57) is satisfied. The factor that is used to scale the theoretical prediction $K = 0.179$. The reason why this error is present might be due to having too little grid points for the interface. This is seen in figure 12. This leads to two problems. The first is the fitting of the arctangent itself. For example at a difference in scattering length of 0.12 nm the width is estimated by the fitting to be 1 μm, while from figure 12 it may be seen that the interface starts at approximately -50 μm and ends at -46 μm. The other half of the problem is that the simulation itself has too little points to simulate the interface accurately.

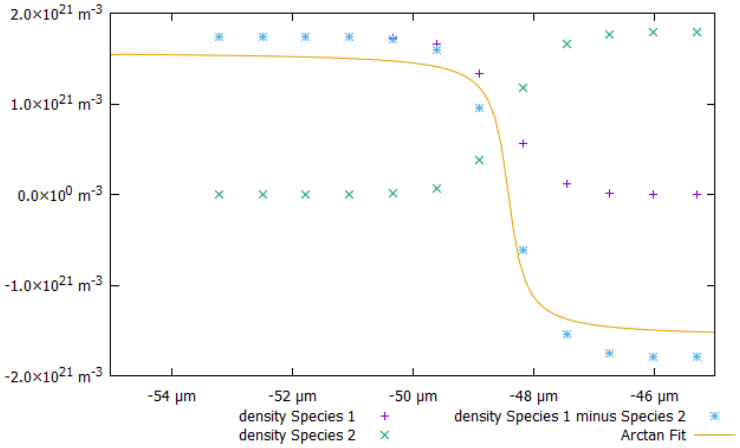

Figure 12: Intersection through the center of the condensate at with: $a_{11} - a_{22} = 0.12$ nm

3.5 Sound waves in the condensate

In order to check if the real time evolution yields correct results a simple simulation is performed. The simulation is done for one spin component. A potential barrier,

$$V_{barier}(y) = \alpha e^{\frac{-y^2}{2\sigma^2}}, \tag{59}$$

is added to the center of the condensate. In this simulation the constants are chosen as $\alpha = 10$ and $\sigma = 5$. The ground state of the system with the potential barrier is computed using imaginary time evolution. Then the barrier is removed and time evolution is begun. The result of this is shown in figure 13.

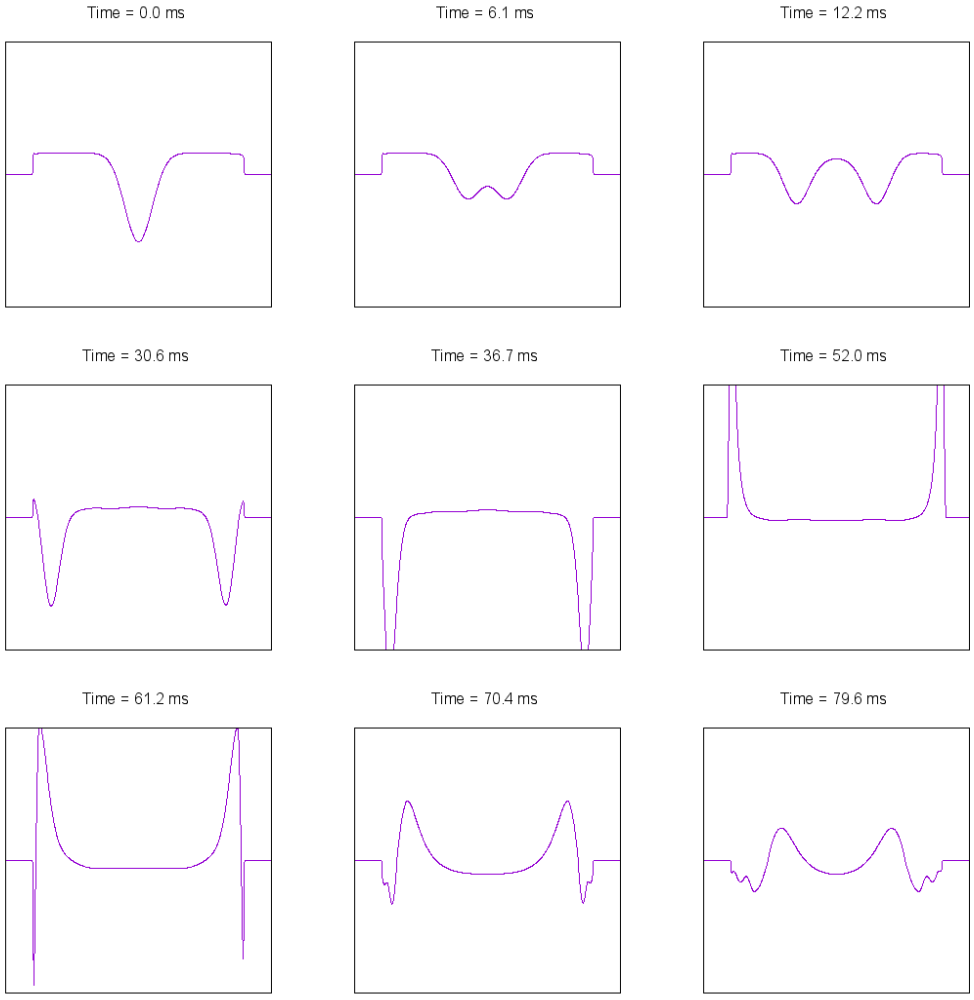

Figure 13: The difference between the current state and the ground state at the line $x = 0$ and $z = 0$. The y axis is the difference between the current state and the ground state and takes values from $-2 \times 10^{19}\,\mathrm{m}^{-3}$ to $2 \times 10^{19}\,\mathrm{m}^{-3}$. The x axis is the position from the origin and take values form $-500\,\mu\mathrm{m}$ to $500\,\mu\mathrm{m}$. The sharp drop near the edges is due to the wave-function decaying exponentially there.

The behavior seen in figure 13 is comparable to that seen in earlier simulations [Pratama(2011)]. The waves in figure 13 propagate to the end of the condensate at which they build up and later reflect as a high density wave instead of a low density wave. The build up is explained by the theoretical prediction for the speed of sound [Smith(2008)]:

$$c_B = \sqrt{\frac{nU_0}{m}}. \tag{60}$$

Because the sound speed is dependent on the density, n, it slows down at the edge of the condensate where the density drops to near zero. This decrease in propagation speed causes the self-steepening of the wave. The reflection with a low density wave may be explained as a reflection at a rigid surface. The end of the condensate is rigid since the energy required to deform the condensate is on a different order than the energy used to make the wave.

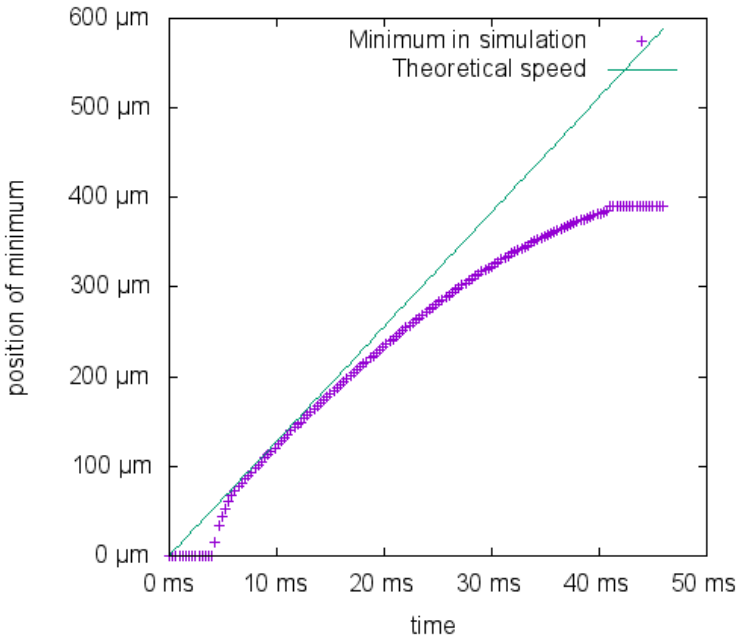

Figure 14: The minimum in the simulation compared to the predicted speed of 0.0128 $\mathrm{m\,s^{-1}}$.

In order to compute the sound speed in the condensate, the position of the minimum is calculated from data of the intersections. These are shown as a function of time in figure 14 combined with the theoretical prediction for the speed of sound in the center of the condensate [Bogoliubov(1947)] :

$$c_B = \sqrt{\frac{\mu}{2m}} = 0.0128\,\mathrm{m\,s^{-1}}. \tag{61}$$

$\mu = 181\hbar\omega_x$ in this simulation. This prediction agrees with the result for a small time, but more is not expected since: The falloff in speed after 20 ms is due to the decrease in density. While the first few entry's in figure 14 are zero since the two waves that originate from the center produce a minimum in zero until they separate.

The ground state seen in figure 13 may be explained from a theoretical perspective. The Thomas-Fermi approximation is used. $V'(x)$ is introduced as the potential of the disturbance and χ as the disturbance in the wave-function. The assumption is made that the distribution of χ does not influence the ground state of ϕ. This assumption is valid when $|\phi|^2 \gg \chi$ this is only true within the condensate. Therefore, the space is restricted to the domain of the condensate in the Thomas-Fermi approximation. Furthermore, the disturbance does not change the amount of particles so: $\int \chi d\boldsymbol{x} = 0$. The energy of the system is written out:

$$E = N \int d\boldsymbol{r}(V(x) + V'(x))(|\phi|^2 + \chi) + \frac{1}{2}\frac{4\pi\hbar^2 N a_{11}}{m}(|\phi|^4 + 2\chi|\phi|^2 + \chi^2). \tag{62}$$

Furthermore, by taking the functional derivative to χ with a Lagrange multiplier A ,that ensures

$\int \chi d\boldsymbol{x} = 0$, of formula 62 a new equation is obtained:

$$A = V(x) + V'(x) + \frac{4\pi\hbar^2 N a_{11}}{m}(|\phi|^2 + \chi). \tag{63}$$

Within the Thomas-Fermi approximation $V(x) + \frac{4\pi\hbar^2 N a_{11}}{m}|\phi|^2$ is constant defined as μ,the chemical potential of the ground state, using this the following is obtained:

$$A = \mu + V'(x) + \frac{4\pi\hbar^2 N a_{11}}{m}\chi, \tag{64}$$

or

$$\chi = \frac{m}{4\pi\hbar^2 N a_{11}}(A - \mu - V'(x)). \tag{65}$$

A is found by using $\int \chi d\boldsymbol{x} = 0$, which implies that
$\int (A - \mu - V'(x))\, d\boldsymbol{x} = 0$. This result explains the distribution of the ground state. In other words: the reason why a small addition of particles in an area spreads homogeneously is because the effective potential,the external potential and self interaction, is constant throughout the condensate.

In a different simulation with different constants $\alpha = 100$ and $\sigma = 1$, strong non-linear behavior is seen. Despite this the speed of sound remains in near perfect agreement to the theoretical result as seen in figure 15. The drop after 10 ms is due to a larger minimum forming behind the initial minimum. In this simulation more than one wave is generated. Once the first waves reach the end of the condensate the simulation becomes chaotic and the chaos spreads trough the condensate.

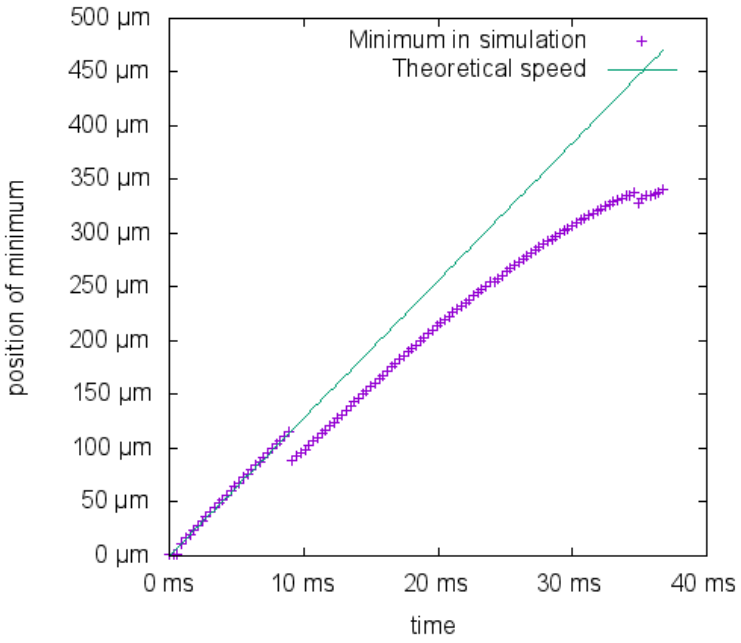

Figure 15: The minimum in the simulation compared to the predicted speed of 0.0128 ms for a much larger deformation. The drop around 10ms is due to a larger minimum forming behind the original minimum. The speed during the first 30 entries is 0.0132 ms, the speed in the 30 entries after the drop 0.01180 ms.

Figure 16: The difference between the current state and the ground state at the line $x = 0$ and $z = 0$. The y axis is the difference between the current state and the ground state and takes values from $-5 \times 10^{19}\,\mathrm{m}^{-3}$ to $5 \times 10^{19}\,\mathrm{m}^{-3}$. The x axis is the position from the origin and take values form $-500\,\mu\mathrm{m}$ to $500\,\mu\mathrm{m}$. The sharp drop near the edges is due to the wave-function decaying exponentially there.

3.6 Time evolution

3.6.1 Symmetric time evolution

The main purpose of the research is to simulate spin-drag behavior of the condensate. In order to do this the condensate is put into a ground state similar to what is seen in figure (3) when time evolution begins. During the time evolution the spin dependent field is flipped in ten milliseconds. Because the interface and healing length become larger as the density is smaller it is necessary to decrease the amount of particles. The amount of particles is decreased to 10^7 particles per species. The length and width of the condensate is adjusted accordingly to 60 μm and 624 μm. The healing length now changes to $\epsilon = 0.27$ μm. Combined with the decrease of the real length in the simulation the difference between 2 mesh points becomes $dy = 0.31$ μm, just above the healing length. Once the time simulation starts the outer part of the first species starts separating and travels up on the sides of the other component. As can be seen in figure 18 the second species moves down around the distortion caused by the first species. After 180 ms the two pieces come close to each other. At approximately 206 ms they combine and a part of them separates and continues moving upward. The pieces that recombined cut of the second species of the condensate so neither can move past each other. At 220 ms the recombined part starts breaking up. At this point the symmetry of the system starts breaking up. This can be seen more accurately in the flow figure 18. During the break up a vortex is generated that travels next to the packet of the first species. The vortex is seen in figure 19.

Furthermore there are flows inside the entire condensate that alternate. In figure 18 there is a flow through the condensate. The flow is mirrored in the other species. In other words there are waves that increase the density in the center and then decrease the density at the center. This is probably a density wave induced by the flipping of the spin dependent force. A very rough estimate gives the frequency of this alternating flow to be 60 ms.

What may be concluded from this simulation is that the species avoid each other. In other words, the condensates do not mix and the movement only happens by sliding the species past each other. Furthermore, a vortex is formed in the condensate that is located on the interface of the two species.

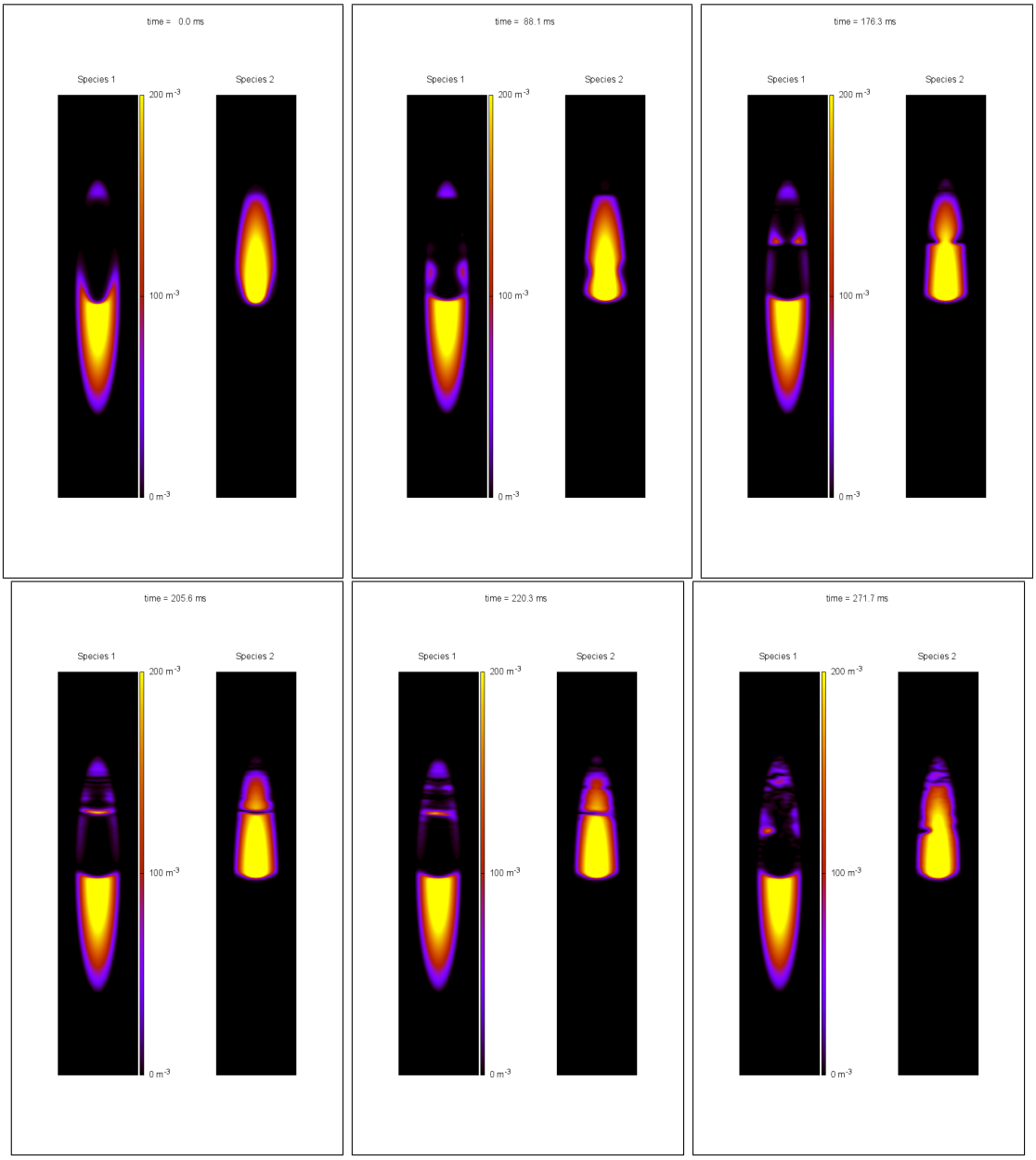

Figure 17: Results of the symmetric time evolution. The width is 60 μm. The height is 600 μm. For clarity the color bar is reduced. The density goes up to 2×10^{20} m^{-3}

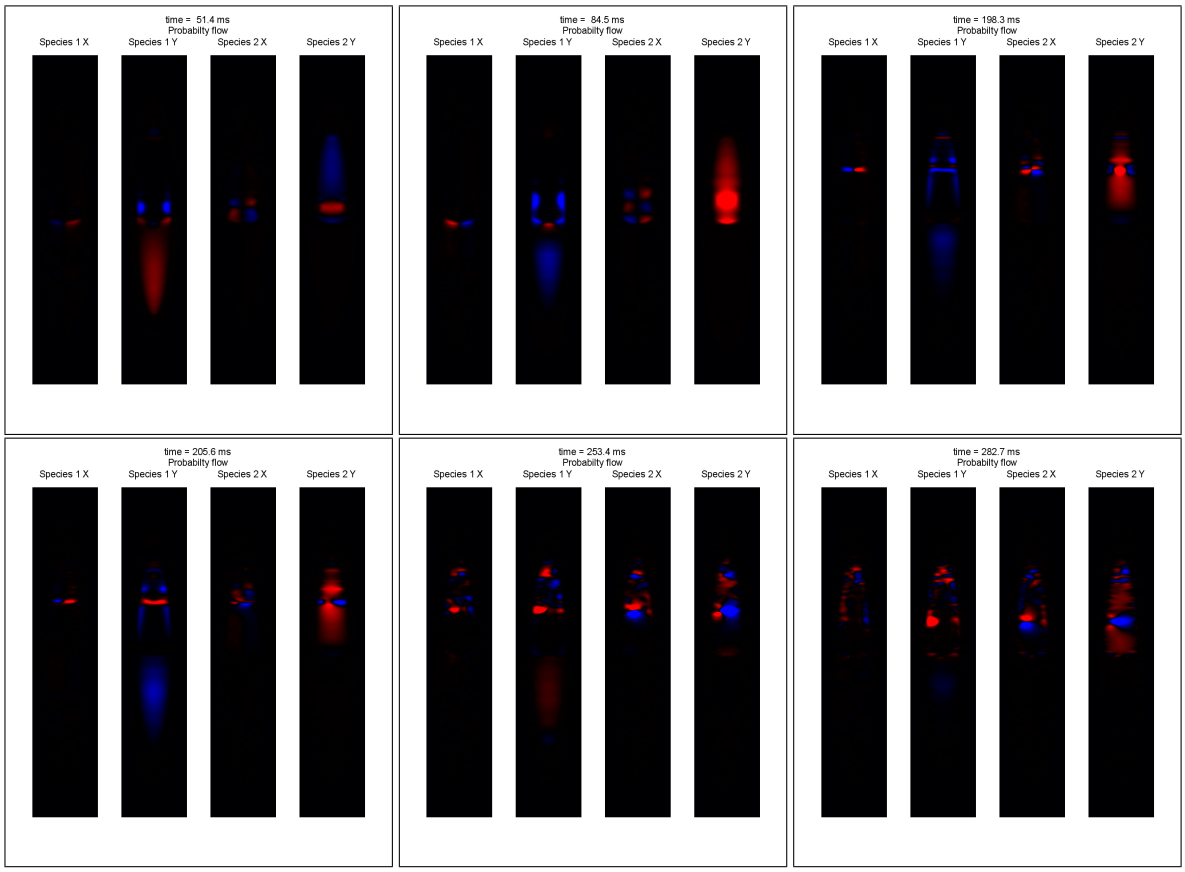

Figure 18: The probability density flow. Blue is movement in the positive direction. Red in the negative direction. So for X blue is movement to the right. Red is movement to the left. In the Y direction blue is up and red is down. The intensity of the color indicates the size of the flow.

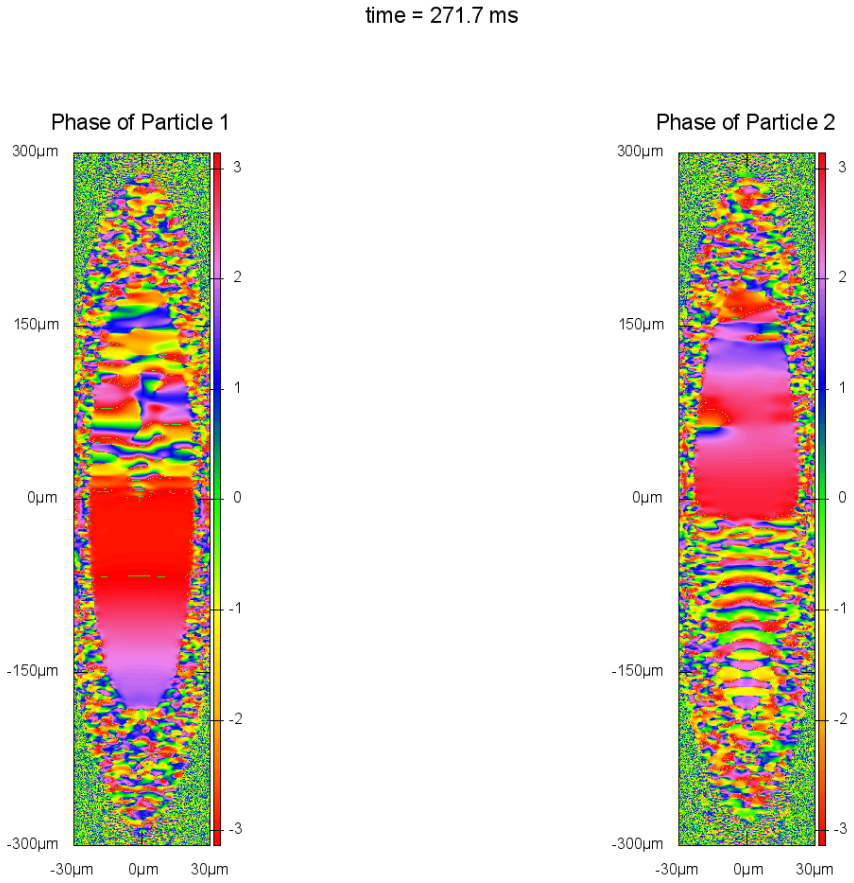

Figure 19: The phase of both species. The phase tends to be random outside of the condensate, because the density is low. In the second species a vortex is seen at approximately $y = 70$ μm at the left side of the condensate. The packet of the first species is at the same location. A vortex is a point where a complete phase is obtained when one moves around it.

3.6.2 Asymmetric time evolution

In the previous section the condensate starts symmetrical and evolves symmetrically for a long time. In a real experiment this is most likely not the case since small perturbations destroy the symmetry. In order to break the symmetry the spin dependent force, M'_x, in the x direction is introduced. For this simulation they are chosen as $M'_y = 0.1$ while $M'_x = 0.02$. In figure 20 the same process occurs as in the symmetrical time evolution. A packet of the first species is formed and starts propagating upwards. This packet reaches the end of the condensate at 160 ms around the same time as the symmetrical case. Unlike the symmetrical case it is allowed to reach the end and stays there. After the packet reaches the end of the condensate the area there becomes volatile. This volatility is probably caused by the presence of free energy that the packet created by traveling up combined with the low density that allows distortions to exist for a small energy cost. After 220 ms the interface at the left side of the condensate shows volatile behavior. This behavior is likely caused by the absence of a thermal cloud. Despite the volatility seen in the later part of the simulation the two species do not mix. Furthermore, the first species remains on the outside of the second species.

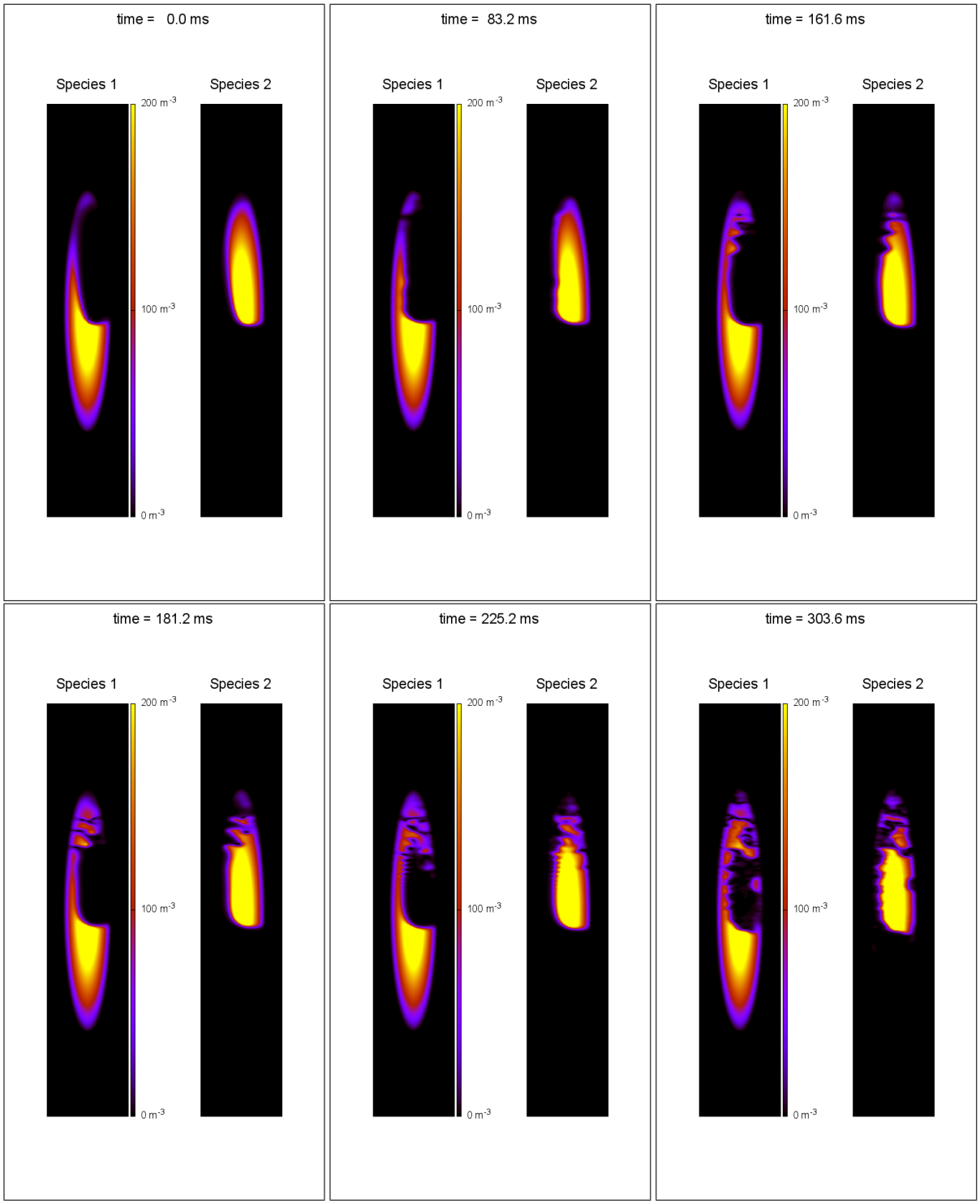

Figure 20: Results of the asymmetric time evolution. The width is 60 μm. The height is 600 μm. For clarity the color bar is reduced. The density goes up to 2×10^{20} m^{-3}

4 Discussion

The choice for η to be a Gaussian distribution, as shown in equation 8, might have been made differently. Since the condensate seen in this thesis is nearly perfectly described by a Thomas-Fermi approximation. The reason why this is not chosen is because the Thomas-Fermi approximation completely discards kinetic energy. As seen in section 2.2 the kinetic energy enforces a lower limit on the height of the condensate. But there is also justification for the current η. Since the x-axis and z-axis are in principle identical, it should be expected that the distribution in the z-axis be approximately the same size as that in the x-axis. As seen in figure 1, η is approximately 30 μm. Taking into account that the distribution in the z-direction is Gaussian so 68% lies within $\frac{30\ \mu\text{m}}{\sqrt{2}} = 21\ \mu$m and 95% lies within $\frac{60\ \mu\text{m}}{\sqrt{2}} = 42\mu$m, which agrees with the size of the condensate in the x direction where it extends to approximately 45 μm. So while η is not perfect, it is approximately the desired size and thus gives the approximate distribution in the z direction.
In the calculation of to equation (22) for η it is chosen not to solve the full equation, but reduce it to 2 cases. In this step a significant error is made in the domain where neither the kinetic energy or self interaction is dominant. As is seen in figure 1 the area where neither is dominant lies outside of the condensate. Therefore this choice is justified for it avoids adding a large computation that must be done on each lattice site for each time-step. The kinetic energy is not entirely left out since it only contributes significantly in a domain where the condensate is not present. The reason why the kinetic energy term is considered at all is that it ensures a lower bound for η. This is important, because in the equations 26 and 27 there is a $\frac{1}{\eta^2}$ term. Leaving η unbounded produces a self reinforcing behavior of removing particles from an area. The end result being all particles located at a single lattice site in the center of the condensate.

The results of the interface do not agree with the theoretical predictions, but the simulation shows the correct behavior for changes in scattering length. In order for this to agree the theoretical result must be multiplied with a factor of $K = 0.179$. This shortfall is probably caused by a too small mesh size combined with the presence of the spin dependent force. The spin dependent force has a large effect on the boundary when the difference in scattering length is small and the interface is large. When the scattering length difference becomes large the interface becomes smaller, the interface is described with less than ten points. In this domain the fit with the arctan does not perfectly describe the interface. By comparing the arctan result with a estimate by looking at the raw data itself a factor of $\frac{1}{4}$ is obtained between the two results. The remaining error is explained by error in the simulation itself. Since the small amount of points create under-sampling. The problem with under-sampling is that large frequency waves can not appear in the Fourier-space. This leads to kinetic energy being smaller then expected.

Another point of discussion is the two dimensional nature of the simulation. The tree dimensional case could not be performed, since it is a large computational task. Each of the dimensions gives extra space to move around other objects. The forming of the interface and bouncing back in figure 17 might not have happened in more dimensions. As seen in the simulation the species form a interface, but when this interface is formed it provides a barrier to mutation of the other species. The other species must pierce trough the interface in the entire z dimension in order to get past the other. If more dimensions are present the interface may be pierced at a smaller surface, allowing more movement.

The last problem that is seen in the simulation is the absence of damping. By performing time evolution on a system that is not in its ground state, it will obtain free energy as the simulation progresses and the system comes closer to the new ground state. All this free energy eventually ends up as solitons or small parts drifting in a domain dominated by the other species. In the a real experiment the thermal cloud acts as a damping.

5 Conclusion

The developed model and simulation are suitable to describe the behavior of a two component Bose-Einstein condensate. This is concluded from the correct prediction of the sound speed in the condensate and correct relation for the width of the interface. The time evolution predicts that the condensate do not mix and tend to slide past each other with a preference of the first species to remain on the outside of the condensate. Furthermore the two species are capable of exerting force on each other as may be seen by the bouncing of the condensate in the symmetrical time evolution. The simulation predicts that the interface is volatile when forces are applied on the condensate, but this effect might be caused by the absence of damping.

6 Outlook

An important addition to the simulation is to introduce dampening. The most obvious way of dampening is to use imaginary time evolution as a dampener. but the problem with this approach is that imaginary time evolution does not conserve particle number so renormalization is required. The effect of the renormalization is that particles disappear in energetically high positions and appear in energetically low positions. Effectually this compromises all of the dynamics of the system since the end result is the renormalization being the main cause of transportation. A better approach might be to simulate the interaction with the thermal cloud. A simpler addition is to run most of the simulation on lower particle number. Since with lower density the healing length of the system becomes larger. This allows a more accurate description of the interface. Furthermore, the sound measurement may be repeated for a two species condensate. The influence of the interface might be interesting to study. At last, it should be possible to create vortices in the simulation, either by imprinting a phase or by "stirring" in the condensate.

References

[Bogoliubov(1947)] N. N. Bogoliubov. On the theory of superfluidity. *J. Phys. USSR*, 11:23–32, 1947.

[Corver(2015)] Jurre Corver. Interfaces in spinor bose-einstein condensates. Bachelor's thesis, University Utrecht, 2015.

[L. Salasnich and Reatto(2002)] A. Parola L. Salasnich and L. Reatto. Effective wave-equations for the dynamics of cigar-shaped and disc-shape bose condensates. *Phys. Rev. A 65*, 2002.

[Matuszewski(2010)] Michał Matuszewski. Ground states of trapped spin-1 condensates in magnetic field. *Phys. Rev. A 82*, 2010.

[Pratama(2011)] S. Pratama. Dynamical simulations of trapped bose-condensed gases at finite temperatures. Master's thesis, University Utrecht, 2011.

[Smith(2008)] C. J. Pethick & H. Smith. *Bose-Einstein condensation in dilute gases.* cambridge university press, second edition, 2008.

[Weizhu Bao and Markowich(2003)] Dieter Jaksch Weizhu Bao and Peter A. Markowich. Numerical solution of the gross–pitaevskii equation for bose–einstein condensation. *Journal of Computational Physics 187*, 2003.